Building and Environment 219 (2022) 109150

Contents lists available at ScienceDirect

Building and Environment

journal homepage: www.elsevier.com/locate/buildenv

Exploration of urbanization characteristics and their effect on the urban thermal environment in Chengdu, China

Wenping Yu [a], Jinan Shi [b], Yuling Fang [a], Aimeng Xiang [a], Xiang Li [a], Chunhong Hu [a], Mingguo Ma [a,*]

[a] Chongqing Jinfo Mountain Karst Ecosystem National Observation and Research Station, School of Geographical Science, Southwest University, No. 2 Tiansheng Road, Beibei District, Chongqing, 400715, China

[b] Software Engineering Institute, Pass College of Chongqing Technology and Business University, No. 593 Jiaotong Road, Hechuan District, Chongqing, 401520, China

ARTICLE INFO

Keywords:
Urban heat island
Urbanization
Sustainability
Land surface change
Land use management

ABSTRACT

As rapid urbanization has drastically and widely altered the Earth's surface, urbanization has become an important contributor to changes in land surface temperature (LST) and the urban thermal environment, which has increasingly become a focus of urban ecologists and environmentalists. The present study used one of the fastest-growing cities in Southwest China, Chengdu city, as an example to explore the urbanization pattern and its effects on surface urban heat islands (SUHIs). To analyze the temporal and spatial characteristics of urban expansion, land use or land cover (LULC) images were classified using a support vector machine (SVM) classifier from Landsat images in 2004–2018, with an overall accuracy of 0.94 and kappa coefficient of 0.90. According to the spatiotemporal LULC changes, Chengdu city expanded at a rapid pace from 80.43 km^2/a to 210.50 km^2/a in 2004–2018, with an increasing reliance on vegetation area conversion. Spatially imbalanced expansion also occurred. The gravity center moved toward the southeast overall, and peripheral circle districts were the main force of Chengdu's urban expansion compared to the slow-expanding core districts. An allometric model was used to analyze the urbanization pattern, and the results indicated that expansion in Chengdu city was far in excess of its corresponding population growth. The SUHI effect in Chengdu mostly deteriorated over time, and SUHI deterioration closely correlated with the urban expansion area rate and expansion intensity. Therefore, excess urbanization at the expense of vegetation decrease damages the urban ecological environment and accelerates SUHI effects, which threaten habitat health and living comfort.

1. Introduction

Rapid urbanization has seriously changed the Earth's surface due to the replacement of natural surfaces, such as vegetation areas, with man-made impervious surfaces, such as concrete and buildings [1–5]. Compared to vegetation surfaces, impervious surfaces emit and absorb more thermal energy, notably alter the surface thermal environment and greatly drive urban heat islands (UHIs), which are one of the most severe ecological and environmental land use or land cover change (LULC-C)-related problems on the global scale [6,7], and impose a non-negligible effect on human health [8,9]. The surface thermal environment manifesting the heat exchange balance between land and atmosphere can be quantified with the land surface temperature (LST). The UHIs effect, a phenomenon in which the temperature in urban areas is higher than other regions [10], reflecting urban surface thermal environment effects, can be quantitatively monitored and dynamically analyzed from the LST parameters, namely, surface UHIs (SUHIs), specifically representing the radiative temperature difference between urban and nonurban surfaces [11,12]. Although many scholars agree that urbanization relatively enhances UHIs effects, previous studies reported inconsistent conclusions due the variety of geographical locations, natural and social environments, and other related factors [9, 13–16]. Therefore, the spatiotemporal effect of urbanization should be further explored in a considered region using a relevant urbanization model and suitable environmental backgrounds.

As one of the fastest urbanizing countries in the past 30 years, China experienced a 2.14% higher urbanization rate than the world average value, and Chinese urban areas are growing by 7.9% per year on average

* Corresponding author.
E-mail addresses: ywpgis2005@swu.edu.cn (W. Yu), shijinan@alu.hit.edu.cn (J. Shi), 18081872257@qq.com (Y. Fang), 2190105449@qq.com (A. Xiang), 1696484237@qq.com (X. Li), 2551511304@qq.com (C. Hu), mmg@swu.edu.cn (M. Ma).

https://doi.org/10.1016/j.buildenv.2022.109150
Received 11 December 2021; Received in revised form 6 April 2022; Accepted 25 April 2022
Available online 6 May 2022

[16,17]. Growth in China may remain the fastest worldwide over the next 50 years or more [18,19]. Accordingly, the thermal environment, especially the SUHI effect, in China is relatively more common and apparent than other regions or countries. This issue has drawn scholars to study the SUHI effect and urbanization in China, but these studies mostly focused on the most well-developed areas or mega-urban agglomerations [7,14,20–22]. Underdeveloped areas in western China have been overlooked [23], and these areas mostly exhibit characteristics of a relatively fragile ecology and high vulnerability to climate change impacts. Therefore, it is necessary to explore urbanization characteristics and their effects in regions that sensitive to global climate changes and easily occurring extreme disasters.

Remote sensing is an efficient method to map and monitor complex regional and global land surface environments [24–26]. With advantage of reasonable spatial resolution and moderate revisiting frequency, moderate-spatial resolution satellite-based remote sensing, such as Landsat series, is widely used to facilitate LULCC monitoring in urban areas [27–29]. Ridd [28] determined that urban areas were generally covered by three material types, vegetation (V), impervious surfaces (I), and soil (S), i.e., the V–I–S model. Changes in impervious surfaces or built-up areas in urban areas are the most obvious responses to human activities, such as human population distribution. Therefore, impervious fraction mapping constitutes a key step in urbanization monitoring. Many studies has employed the V–I–S model for image classification to monitor LULCCs and extract impervious cover in urban environments to further explore urbanization based on series classification images [24–26,30,31]. Based on the V–I–S model, researchers have continuously developed classification methods to detect impervious surfaces, such as the decision tree classifier [32], maximum likelihood classifier [25], spectral mixture analysis (SMA) and improved methods [26,28,33]. However, accurate land use type detection, especially impervious surfaces, remains a challenge due to the highly complicated surfaces in urban environments.

The medium-resolution remote-sensing LST data commonly have advantages of suitable spatial resolution and ready accessibility to explore the urban SHUI effect. The LST retrieved from satellite-based thermal infrared (TIR) data always exhibits high accuracy, and corresponding retrieval methods, such as the single-channel, split-window (SW) and multichannel methods, have reached a relatively mature development stage [34–41]. LST data retrieved from TIR data recorded by moderate-spatial resolution sensors, such as Advance Space-borne Thermal Emission and Reflection Radiance (ASTER), Thematic Mapper (TM) and Thermal Infrared (TIR) sensors, have enabled exploration of SUHI effects at the urban scale [10,42–45]. Landsat constellation has been emphasized very important to the SUHI knowledge by Zhou et al. [12] and they have indicated that almost 53% of researchers have use either one or multiple Landsat images in their SUHI studies.

The present study selected an economic and trade hub in Southwest China, Chengdu, as a case study to explore the spatiotemporal characteristics of urbanization, and the SUHI effect change tendency was considered. Furthermore, as feedback, better understanding of the effects of land use, especially impervious surface/built-up areas, will help urban land developers and planners regulate urban land and urban thermal environment planning. The land use maps and corresponding LST images for Chengdu city from 2004 to 2018 used in this study were obtained from Landsat series images and readily and historically available and economic data. The classifier and retrieval method are detailed in the methodology section, followed by the results and a discussion of urbanization in Chengdu city and its relationship with SUHI effects considering spatiotemporal changes. Finally, the Conclusion section provides a summary.

2. Materials and methods

2.1. Study area and data

Chengdu (30°05′N-31°26′, 102°54′E−104°53′E) is the capital of Sichuan Province in Southwest China, and the total area is approximately 12390 km^2. With a typical continental monsoon climate in the northern temperate zone, the average temperature ranges from 5 °C in winter to 26 °C in summer. The annual precipitation reaches approximately 900 mm, and rainfall is primarily concentrated in July and August. Chengdu city is one of the most crowded cities in Southwest China, and has been approved by the State Council as the national high-tech and logistics base and business and transportation hub since 2015. This study focuses on the urban development area of Chengdu (Fig. 1), covering approximately 3677 km^2, and considers 11 districts: five central districts in the first circle, Jinjiang District (JJ), Wuhou District (WH), Qingyang District (QY), Jinniu District (JN), Chenghua District (CH); and six emerging suburban districts in the second circle, Pidu District (PD), Shuangliu District (SL), Wenjiang District (WJ), Xindu District (XD), Longquanyi District (LQY), and Qingbaijiang District (QBJ). This study examined Chengdu city, in which the landscape is mostly flat, with an average altitude of 524 m, ranging from 437 to 1042 m, as shown in Fig. 1(c). There are few hills with basic trends along the eastern boundary of Chengdu city.

Based on a previous study, Landsat data are a very effective and easily accessible satellite-based data source for land use mapping and thermal environment monitoring in urban areas [6,15,16]. The data collected in this study included Landsat 5 and 8 images, as detailed in Table 1. Since frequent clouds occurring in the Chengdu city, considering the cloud cover percentage (an acceptable level lower than 5%) and time space to implement the study, only four Landsat images acquired in 2004, 2009, 2013 and 2018 were selected and downloaded from https://earthexplorer.usgs.gov/, including packaged multispectral (MS) data (including visible and near- and mid-infrared bands) and TIR data (Band 6 in Landsat 5, and Bands 10 and 11 in Landsat 8). The Landsat 8 images in Collection 1 were selected in this study, which has been implemented TIRs stray light correction and updated since 2017 [46–48].

To explore urbanization characteristics and their effects on the thermal environment in urban areas, the study was implemented following the flowchart shown in Fig. 2. The process was divided into two sections: urbanization detection via LULCC and thermal environment change characterization considering LST variations in the study area. Since the Landsat images are obtained at about 11 a.m. (detailed in the fourth column of Table 1), the instantaneous SUHI effect is used to explore the urban thermal environment in this study, and furtherly discuss the urban thermal environment changes from 2004 to 2018. Essential preprocessing of the Landsat images, involving Google Earth imagery-based geometrical correction, radiometric calibration, and atmospheric correction, was performed before land use classification and LST retrieval. Because the MS and TIR bands exhibited different spatial resolutions, the images were all resampled to 30 spatial resolutions during preprocessing. Land use classification and LST retrieval are the key steps after image preprocessing. The LULC in the present study was classified from color images composited with the normalized difference vegetation index (NDVI), normalized difference built-up index (NDBI) and modified normalized difference water index (MNDWI) bands. The main steps implemented in this study are detailed below. To examine the rationality of city expansion, population information on the study area was selected from the Total Registered Households and Population over Years section of the 2019 Chengdu Statistical Yearbook.

2.2. LULC classification

Compared to other regions, a city is broadly defined as a permanent large settlement [16]. A four-LULC type classification system, including

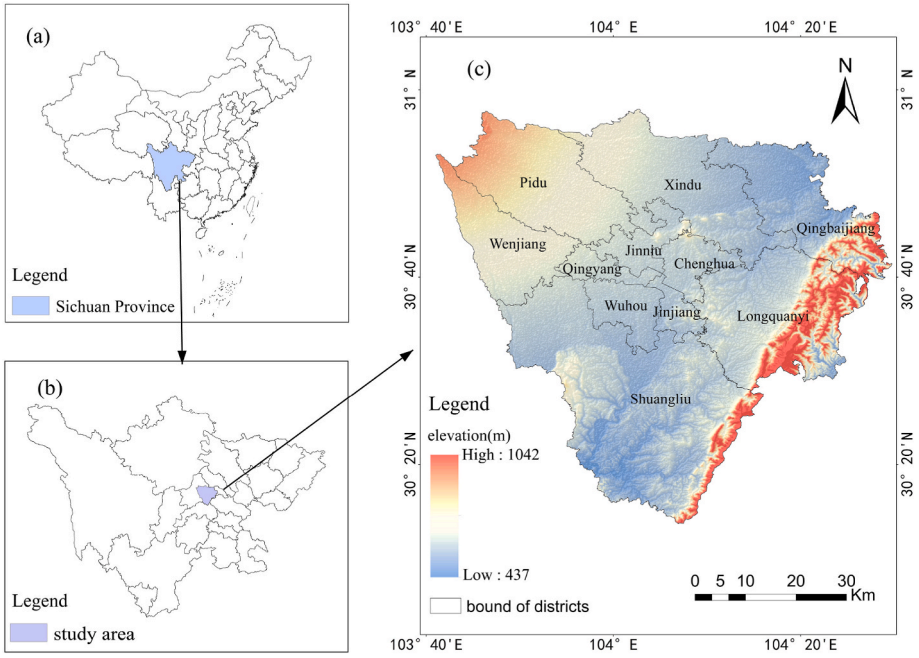

Fig. 1. Location maps of the study area.

Table 1
Details of the Landsat images in this study.

Satellite	Path/row	Acquisition date	Local time	Spatial resolution (MS/TIR)	Cloud cover (%)
Landsat 5	129/39	2004-12-07	11:19	30 m/120 m	0.12
Landsat 5	129/39	2009-03-24	11:20	30 m/120 m	0
Landsat 8	129/39	2013-04-20	11:35	30 m/100 m	4.66
Landsat 8	129/39	2018-04-18	11:32	30 m/100 m	0.4

water body, vegetation, impervious surface/built-up, and bare soil areas, was defined in the present study based on the land cover biophysical characteristics of Chengdu city and previous research, especially the V–I–S model. Impervious surface expansion is generally the most obvious representation of urban expansion in a city. Therefore, it is essential to precisely detect impervious surfaces. To differentiate the LULC from Landsat MS data, especially impervious surfaces in bare soil areas, color images were constructed with three index bands: NDVI, NDBI and MNDWI bands. The NDVI is a numerical indicator calculated by the visible and near-infrared bands of remote sensing data and has been broadly adopted to identify live green vegetation [49,50]. Zha et al. [51] first proposed the NDBI to automatically map urban areas using Landsat data, and it has remained a sufficient indicator in the identification of impervious areas. Han-Qiu [52] established the MNDWI based on the normalized difference water index (NDWI) algorithm first proposed by McFeeters [53], which easily extracts water bodies from other background objects [54]. These three indicators, NDVI, NDBI, and MNDWI, were calculated with Equations (1)–(3):

$$NDVI = \frac{NIR - R}{NIR + R} \tag{1}$$

$$NDBI = \frac{MIR - NIR}{MIR + NIR} \tag{2}$$

$$MNDWI = \frac{G - MIR}{G + MIR} \tag{3}$$

where$G$, R, NIR, and MIR are the green band radiance, red band radiance, NIR band radiance, and mid-infrared band radiance, respectively, in Landsat MS images, which were corrected and calibrated during image preprocessing. Composited images of the study area are shown in Fig. 3.

Training regions that were representative of the four LULC types were first selected from the known area based on the characteristics of the four types referring to Google Earth images. The support vector machine (SVM) classifier was used as a typical and dependable supervised classification algorithm to enable a computer system to automatically recognize pixels with the same feature and map LULC images. The classification results in 2018 were evaluated according to the 2018 high-spatial resolution Google Earth image with a spatial resolution greater than 1 m. This process randomly generated 791 sample points according to the area size of each type in the LULC images: 422 points for impervious surfaces, 315 points for vegetation areas, 38 points for bare soil areas, and 16 points for water bodies. The land use types at these points were individually determined via manual visual interpretation in the high-resolution Google Earth imagery, which were used as validation samples. The accuracy of the 2018 classification map was considered the accuracy of the classification method used because Google Earth imagery was hardly available in accordance with the Landsat images in this study. The total classification accuracy was estimated by the overall accuracy (OA, Equation (4)) and kappa coefficient (K_a, Equation (5)), and the classification accuracy of land use i was calculated by the producer accuracy (PA_i, Equation (6)) and user accuracy (UA_i, Equation (7)).

$$OA = \frac{\sum_{i}^{4} M_i}{N} \tag{4}$$

$$Ka = \frac{OA - \frac{\sum_{i}^{4} P_i U_i}{N^2}}{1 - \frac{\sum_{i}^{4} P_i U_i}{N^2}} \tag{5}$$

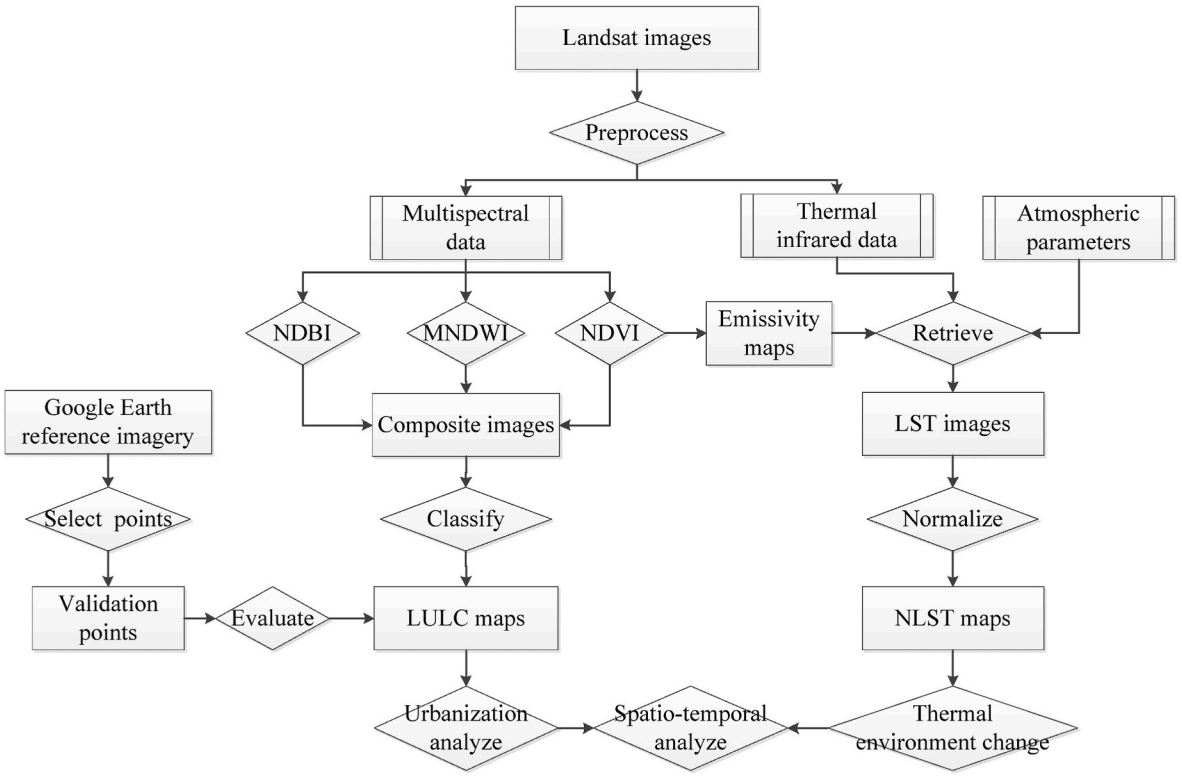

Fig. 2. Flow chart to detect urbanization and urban thermal environment changes in Chengdu city and further explore their relationship in advance.

$$PA_i = \frac{M_i}{P_i} \tag{6}$$

$$UA_i = \frac{M_i}{U_i} \tag{7}$$

where M_i denotes the number of points correctly classified into category i, N is the total number of selected validated points, P_i is the number of sample points belonging to land use i according to reference Google Earth imagery, and U_i is the number of points classified into land use i among the classification results.

2.3. Conversion of LULC

Based on the LULC maps, an LULC transition matrix (Equation (8)) was calculated to quantitatively describe the conversion and direction among the various LULC types. Because the LULC maps were obtained at four time points, three transition matrices during the 2004–2009, 2009–2013, and 2013–2018 periods for Chengdu city were summarized from spatial LULC transition maps.

$$A_{trans} = \begin{bmatrix} A_{11} & \cdots & A_{1n} \\ \vdots & \ddots & \vdots \\ A_{n1} & \cdots & A_{nn} \end{bmatrix} \tag{8}$$

where n is the total number of LULC types, A_{ij} is a term of the matrix A_{trans} and represents the area transferring from LULC types i to j during the period from t to t+1.

2.4. Quantification of the spatiotemporal characteristics of urban expansion

Based on the LULC maps from 2004 to 2018, the areas of the four land use types were calculated in ArcMap software, especially impervious surface/built-up areas, and any increase clearly represented urban expansion. Based on the impervious area, three indicators, the urbanization growth index (UGI), change rate of impervious surface/built-up areas (R_t), and urbanization intensity index (UII), were employed to quantify urbanization in Chengdu city, defined as follows [55]:

$$UGI = \frac{s_{Y_2} - s_{Y_1}}{\Delta Y} \tag{9}$$

$$R_t = \frac{s_{Y_2} - s_{Y_1}}{s_{Y_1}} \times 100 \tag{10}$$

$$UII = \frac{s_{Y_2} - s_{Y_1}}{s_{Y_1}} * \frac{1}{\Delta Y} \times 100 \tag{11}$$

where s_{Y_2} and s_{Y_1} are the impervious surface/built-up areas in Y_2 and Y_1, respectively, and ΔY is the interval from Y_2 to Y_1. To explore the directional characteristics of expansion in space, the area contributions of the eight directions to urbanization were calculated based on impervious surface maps extracted from LULC classification maps. The contribution in the D_i direction was determined as follows:

$$\omega = \frac{s_{D_i}}{s} \tag{12}$$

where s is the total expansion area of impervious surfaces, and s_{D_i} is the area increase along direction D_i. Since imbalanced spatial expansion can lead to a direction offset for the city center, the centroid method was applied to obtain the overall spatial movement of the Chengdu city center, as follows:

$$X_t = \sum_{i=1}^{n}(C_{it} * X_{it}) \Big/ \sum_{i=1}^{n} C_{it} \tag{13}$$

$$Y_t = \sum_{i=1}^{n}(C_{it} * Y_{it}) \Big/ \sum_{i=1}^{n} C_{it} \tag{14}$$

where X_t and Y_t are the x- and y-coordinate values, respectively, of the impervious surface center at$t$, and C_{it} is the area of impervious surface i,

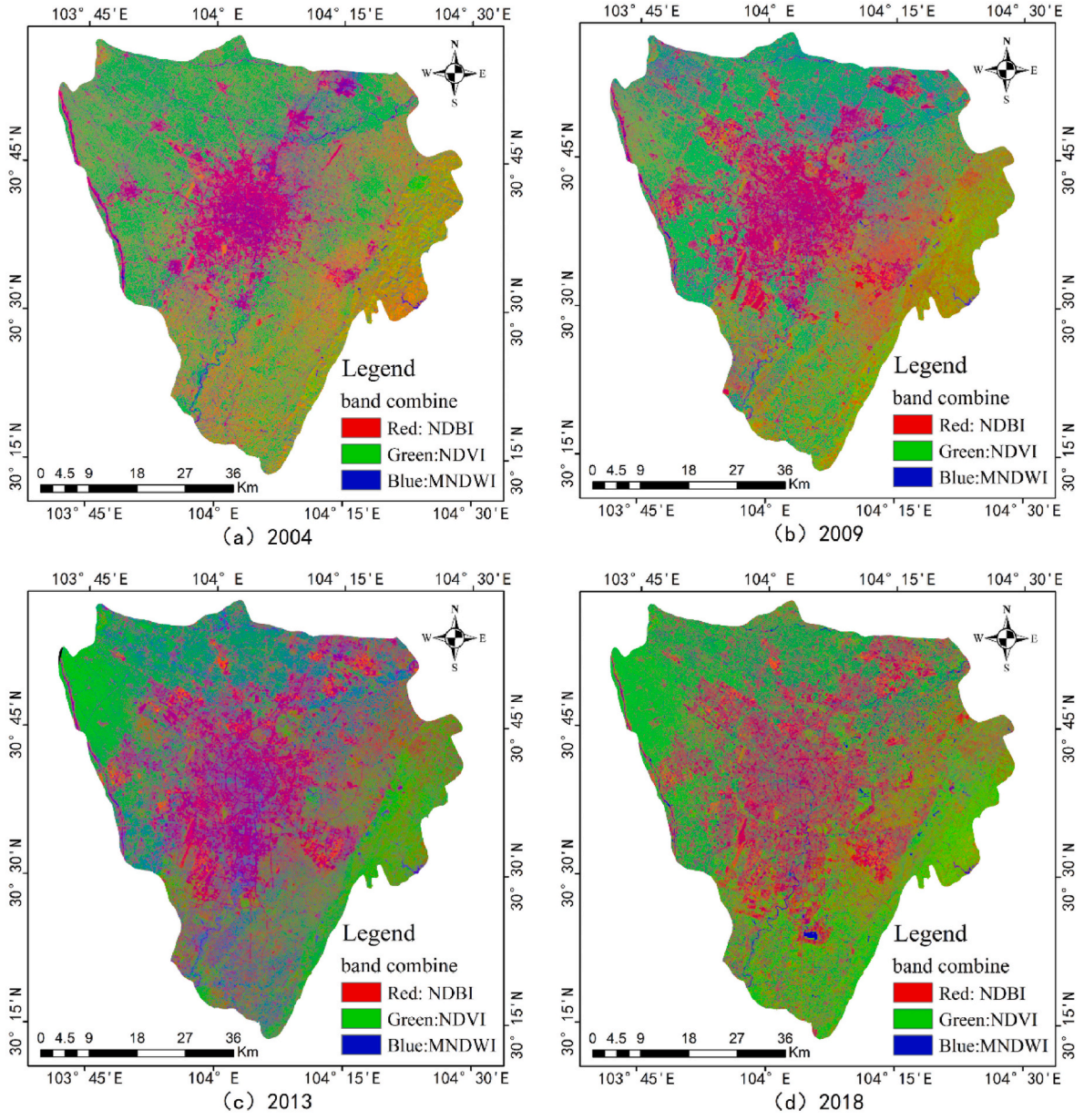

Fig. 3. Index-composited images of the study area. (a), (b), (c), and (d) show images in 2004, 2009, 2013, and 2018.

whose subcenter is (X_{it}, Y_{it}) at t.

City expansion exhibits a close relationship with population growth, and a good compatibility between these factors is expected for rational land use planning. The allometric model, as expressed in Equation (15), first proposed in the biological field and subsequently introduced into the human geography field [56,57], was employed to examine the expansion rationality in Chengdu city.

$$A = aP^b \tag{15}$$

where A is the impervious surface/built-up area, P is the urban area population, and a and b are regression parameters. In the equation, b is a key parameter that indicates the allometric relationship between A and P. Previous studies on urban areas in China indicated: when $b = 0.9$, the expansion of built-up areas fit well with the increase in population; when $b < 0.9$, negative allometric growth occurs, which means that the expansion of built-up areas is deficient for the increase in the corresponding urban population; and when $b > 0.9$, positive allometric growth occurs, which suggests that built-up area expansion is superfluous to the increase in the corresponding urban population [58–60].

2.5. LST retrieval and normalization

Landsat 5 and 8 TIR data were used to retrieve the LST in Chengdu city. There was one TIR (Band 6) band in the Landsat 5 data, and also one TIR band (Band 10) in the Landsat 8 data without potential calibration risk due to the out-of-field stray light effect. Therefore, the radiation transfer model (RTM) in the TIR band (Equation (16)) was used to retrieve the LST from Landsat 5 and Landsat 8 data. Based on Equation (16), the land surface emissivity (LSE, ε_λ) and three atmospheric parameters, τ_λ, $L_\lambda^{atm\downarrow}$, and $L_\lambda^{atm\uparrow}$, are necessary for LST retrieval from $B(\lambda, T_s)$. Following Planck's law for blackbodies, for a given $B(\lambda, T_s)$, LST (T_s) is the only variable in a certain TIR band with a known λ. According to the metadata of Landsat 5 and Landsat 8 images, the three atmospheric parameters of each Landsat image were obtained from the NASA website (https://atmcorr.gsfc.nasa.gov/), and the LSE was retrieved by the NDVI threshold algorithm which was formulated by Sobrino and Raissouni [61] and has already been applied to various sensors data for its

simplicity [61–64].

$$L_{\lambda}^{Sensor} = \left[\varepsilon_{\lambda} * B\left(\lambda, T_s\right) + \left(1 - \varepsilon_{\lambda}\right) * L_{\lambda}^{atm\downarrow}\right] * \tau_{\lambda} + L_{\lambda}^{atm\uparrow} \quad (16)$$

The LST exhibits high temporal heterogeneity, and the LST images in this study were not obtained at same months of year (seeing Table 1) for the data quality control over cloud-cover in images. Therefore, to avoid biases caused by temperature variation over time, the normalized LST, as the thermal environment index (TEI) [65], was employed to analyze the urban thermal environment in this study as follows:

$$T_{norm\_i} = \frac{T_{s\_i} - T_{s\_min}}{T_{s\_max} - T_{s\_min}} \times 100 \quad (17)$$

where T_{norm_i} is the normalized LST value in the i-th pixel, T_{s_max} and T_{s_min} are the maximum and minimum LSTs, respectively, in each LST image, that are commonly found in impervious and waterbody pixels, respectively, and T_{s_i} is the LST value in the i-th pixel. Therefore, the normalized LST in the pixels ranged from 0 to 100.

2.6. Thermal environment change detection

Based on the TEI, heat island grades were defined to detect changes in the urban thermal environment and SUHIs with urban expansion in Chengdu city from 2004 to 2018. The heat island grades [66,67] ranged from 1 to 6 (Table 2) according to the mean (Equation (18)) and standard deviation (STD, Equation (19)) of the normalized LST images.

$$u = \frac{\sum_{i=1}^{n} T_{norm\_i}}{n} \quad (18)$$

$$STD = \sqrt{\frac{\sum_{i=1}^{n} \left(T_{norm_i - u}\right)^2}{n}} \quad (19)$$

where n is the total number of pixels in the normalized LST image, and u and STD are the mean and standard deviation, respectively.

3. Results and discussion

3.1. Detection of LULC changes

The classification accuracy was evaluated considering 791 points that were randomly selected from the 2018 LULC maps and reclassified via manual visual interpretation based on the 2018 high-resolution Google Earth image. A class confusion matrix was calculated between the LULC classification results and manual visual interpretation reclassification results. The overall evaluation summarized from the class confusion matrix indicated that the classifier performed well with an overall accuracy of 0.94 and kappa coefficient of 0.90. The producer and user accuracies of each land use type were calculated, as listed in Table 3. Except for bare soil, the producer accuracy of the other three types was higher than 87%. The user accuracy of all land cover types was higher than 91%. Although the spectra of bare soil areas and built-up/impervious surfaces exhibited high similarity that commonly caused a lower distinguishability, the producer and user accuracies were higher than 78.9%, and the accuracy of built-up/impervious surfaces, which was the main focus in this study, was higher than 91%. Therefore, the SVM classifier based on the images composited with the three indicators was effective in the study area and performed sufficiently to explore the research issue.

Table 2
Heat island grade levels.

Interval	Level	Thermal environment description
[0, u-1.5*STD)	1	Strong cold island zone
[u-1.5*STD, u-0.75*STD)	2	General cold island zone
[u-0.75*STD, u)	3	Colder mid-temperature zone
[u, u+0.75*STD)	4	Hotter mid-temperature zone
[u+0.75*STD, u+1.5*STD)	5	General heat island zone
[u+1.5*STD, 1]	6	Strong heat island zone

Table 3
LULC classification evaluation.

Evaluation indicator	Built-up	Vegetation	Bare soil	Water body
Producer accuracy	99.76	89.52	78.95	87.50
User accuracy	91.13	99.65	93.75	99.99

Based on the 2004, 2009, 2013, and 2018 LULC maps, LULC changes were detected by the proportion of the changing parts to the total area of Chengdu city, as shown in Fig. 4. Fig. 4 indicates that the LULC change proportion was the lowest from 2009 to 2013 at 11.30% and was higher during the other two periods, 2004–2009 (32.57%) and 2013–2018 (28.63%). Impervious surfaces were the only LULC type that continuously increased from 2004 to 2018. Expansion stabilized during the 2004–2009 and 2009–2013 periods and boomed from 2013 to 2018. Bare soil in Chengdu city was the only LULC type in which the area continuously decreased. The vegetation area change percentage exhibited larger fluctuations with an increase of 33% from 2004 to 2009, −31% from 2009 to 2013, and −43% from 2013 to 2018. In contrast, the water body area changed slightly from 2004 to 2018 (see Fig. 4).

To explore the details of LULC changes and further examine the LULC conversion trend and intensity, a transition matrix of LULC changes during the different periods was calculated, as summarized in Table 4. The transition matrix revealed that the LULC in Chengdu city changed dramatically from 2004 to 2018, especially the conversion of impervious surface/built-up, vegetation, and bare soil areas. From 2004 to 2009, 1241.94 km^2 of bare soil, ~79% of its area in 2004, was converted into other LULC types, primarily vegetation (~77%) and impervious surface/built-up areas (~22%), which was the largest area conversion during this period. The conversions from vegetation and impervious surface/built-up areas were 78.17 and 282.53 km^2, respectively, which accounted for less than 20% (19.9% and 15.5%, respectively) of their areas in 2004. Impervious surface/built-up areas were primarily converted into vegetation areas, which occupied 86% of its conversion area. Meanwhile, vegetation areas were largely occupied by impervious surface/built-up (167.32 km^2) and bare soil (112.78 km^2) areas. The net area converted among these three LULC types reached 269.30 km^2 (impervious surface/built-up areas from bare soil areas), 99.89 km^2 (impervious surface/built-up areas from vegetation areas) and 848.6 km^2 (vegetation areas from bare soil areas). During the 2004–2009 period, compared to a decreased bare soil area of 1117.45 km^2, impervious surface/built-up and vegetation areas increased 402.16 and 795.61 km^2, respectively. Furthermore, ~67% and ~25% of the

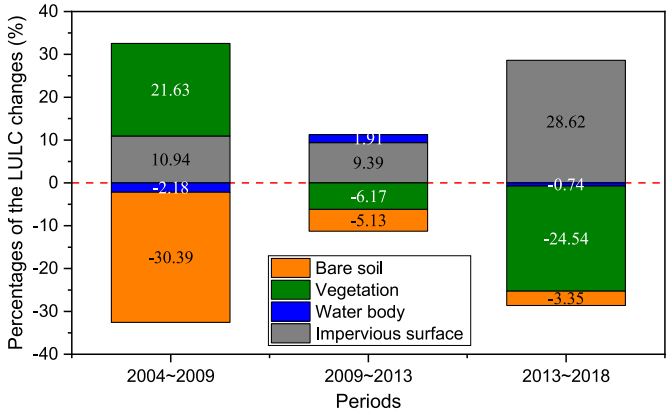

Fig. 4. LULC change percentages during the different time periods.

Table 4
Conversion matrix of the LULC from 2004 to 2018 (unit: km^2).

		2009			
		Built-up	Water body	Vegetation	Bare soil
2004	Built-up	313.53	2.94	67.43	7.81
	Water body	35.91	10.31	49.33	3.91
	Vegetation	167.32	2.43	1329.83	112.78
	Bare Soil	277.11	3.46	961.38	332.04
2009		**2013**			
		Built-up	Water body	Vegetation	Bare soil
	Built-up	608.16	18.36	130.48	36.86
	Water body	3.45	11.88	3.52	0.29
	Vegetation	457.66	55.25	1730.73	164.33
	Bare Soil	69.92	3.79	316.44	66.38
2013		**2018**			
		Built-up	Water body	Vegetation	Bare soil
	Built-up	1033.48	10.29	72.26	23.16
	Water body	36.41	32.40	19.21	1.26
	Vegetation	927.98	18.29	1158.46	76.44
	Bare Soil	193.83	1.26	28.80	43.96

impervious surface/built-up area increase was converted from bare soil and vegetation areas, respectively. Moreover, the area converted from bare soil not only compensated for the vegetation area loss that converted into impervious surface/built-up areas but also accounted for nearly 100% of the vegetation increase.

During the 2009–2013 and 2013–2018 periods, the LULC change rates were lower than the rate from 2004 to 2009, as indicated by Fig. 4. Similarly, the main LULC type conversion also occurred among impervious surface/built-up, vegetation and bare soil areas. From 2009 to 2013, 457.66 km^2 of vegetation area was converted into impervious surface/built-up areas, accounting for ~68% of the vegetation conversion. As a compensation, 316.44 km^2 of vegetation area was converted from bare soil areas, ~81% of the bare soil conversion. Therefore, 95% of the impervious surface/built-up area increase from 2009 to 2013 was derived from a net area of 327.17 km^2 that was converted from vegetation into impervious surface/built-up areas. Despite the bare soil-related compensation, the vegetation area decreased 226.79 km^2. The impervious surface/built-up area increase tripled between 2009-2013 and 2013–2018. Of this notable increase, ~81% (855.71 km^2) was converted from vegetation areas, and the remainder was mostly from bare soil. Compared to the 2009–2013 period, conversion among all of the LULC types occurred from other LULC types into impervious surface/built-up areas, as shown in Fig. 4 and Table 4. Moreover, the compensation phenomenon (conversion from bare soil into vegetation) hardly occurred, with a net conversion area of 5.65 km^2 from bare soil into vegetation.

The LULC changes during the three periods clearly revealed that impervious surface/built-up areas continuously, and even dramatically, increased, especially from 2013 to 2018, and expansion increasingly relied on the net conversion area from vegetation. In contrast, the vegetation area shifted from a considerable increase to a notable decrease due to the area loss primarily into impervious surface/built-up areas and a sharp reduction in compensation from bare soil. Vegetation generally covers arable land, woodlands and grasslands, which are crucial to the ecological environment and grain yield. Therefore, rapid urbanization in Chengdu city, as indicated by impervious surface/built-up area expansion, directly threatens the city's ecological environment and food security.

3.2. Analysis of urban sprawl spatiotemporal characteristics

Urbanization in this study was analyzed from impervious surface expansion in the city. Fig. 5 and Table 5 indicate the spatial expansion from 2004 to 2018. Spatial expansion in Chengdu city (Fig. 5), as

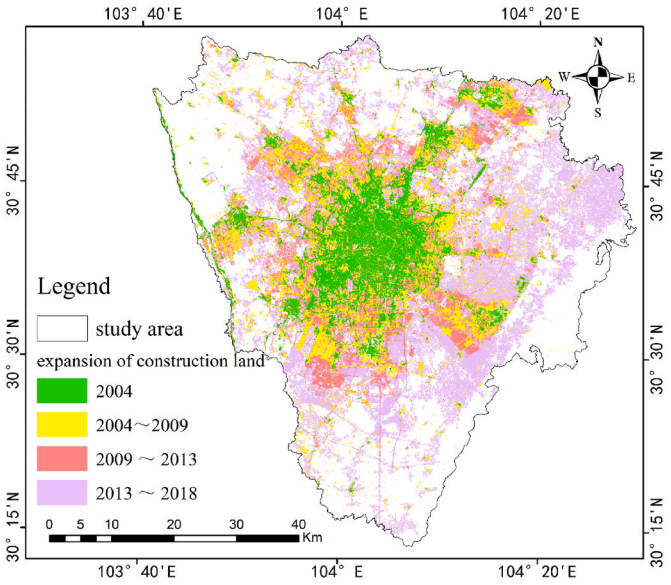

Fig. 5. Impervious surface expansion in Chengdu city.

Table 5
Impervious surface/built-up area expansion rate and intensity.

Periods	Built-up area increase (km^2)	UGI (km^2/a)	R_t (%)	UII (%)
2004–2009	402.16	80.43	102.67%	20.53%
2009–2013	345.33	86.33	43.50%	10.88%
2013–2018	1052.51	210.50	92.39%	18.48%

indicated by impervious surface/built-up area expansion, basically occurred around the main urban area and point-axis new urban district from 2004 to 2018. From 2004 to 2013, the urban area expanded outward from the city center annularly and was primarily characterized by cooperative development and renewal. The earlier built-up area increase remained relatively stable, at 402.16 km^2 from 2004 to 2009 and 345.33 km^2 from 2009 to 2013, and the increase primarily depended on bare soil conversion, especially from 2004 to 2009. Then, from 2013 to 2018, the city experienced high-speed denotative expansion, and the built-up area increase reached 1052.51 km^2 over the area increase sum during the first two periods. The UGI in Table 5 clearly indicates that the average expansion area steadily increased annually, with leapfrog growth from 2013 to 2018. The UGI reached 210.50 km^2/a, more than twice the UGI during the first two periods. The urbanization intensity in Chengdu city, which was characterized by the change rate of impervious surface/built-up areas (R_t) and UII in Table 5, decelerated between 2004-2009 and 2009–2013 then increased from 2013 to 2018.

Fig. 6 clearly shows that expansion in Chengdu city exhibited a spatial tendency over time. From 2004 to 2009, the two greatest contributions to city expansion originated from the northwest and northeast, with contribution rates of 17.38% and 14.77%, respectively. The northern part of Chengdu city contributed only 6.98%, which was much lower than the other relatively adjacent parts. In the other two stages, expansion exhibited a higher orientation and was primarily dominated by four directions: from 2009 to 2013, the northwest, west, southwest, and south directions, and from 2013 to 2018, the northeast, east, southeast, and south directions. Therefore, urbanization in Chengdu city occurred dramatically uneven in its scope and time scale from 2004 to 2018, especially from 2013 to 2018, when expansion dominated toward the east and south, probably followed urban spatial development policies: moving to the east, spreading in the south, holding in the west, rectifying in the north, and optimizing in the center. Different expansions occurred in the 11 districts in the Chengdu main city. SL is clearly identified in Fig. 7 by its highly notable impervious surface/built-up

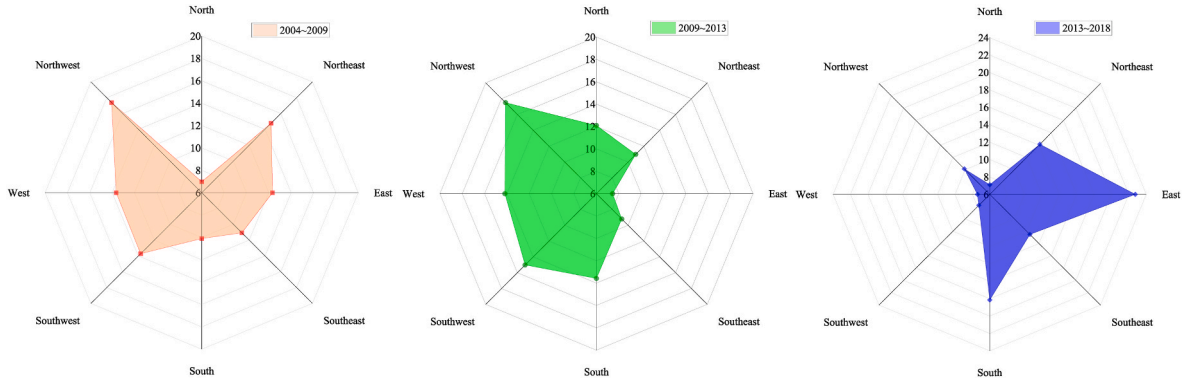

Fig. 6. Expansion area contribution rate in the different directions.

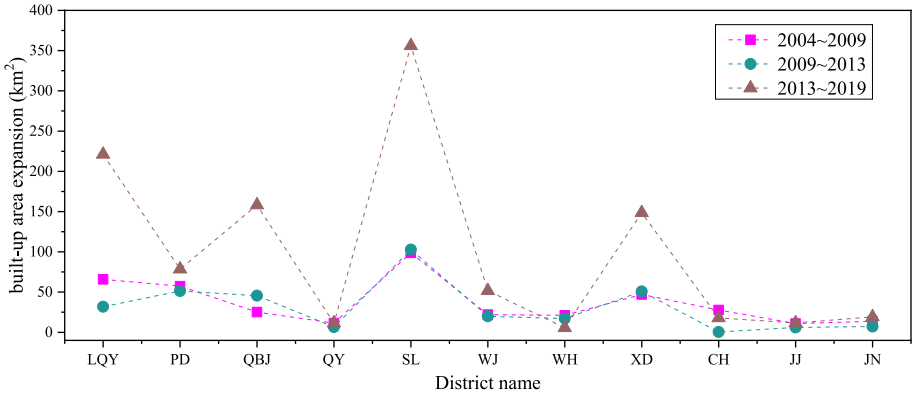

Fig. 7. Impervious surface expansion in each district.

area expansion during the three periods, especially from 2013 to 2018. Along with SL, XD, PD, and LQY are generally districts with an expansion area larger than the average area during the three periods. JJ and QY were also distinguished by their smaller impervious surface area expansion. The gaps between the largest and smallest area expansions grew over time, from 87.80 km^2 in 2004– 2009 and 102.42 km^2 in 2009–2013 to 350.29 km^2 in 2013– 2019.

Depending on the contribution rate of each district (Fig. 8), all of the main districts in Chengdu city were graded into three levels: most powerful expansion, SL district; basically stagnant districts, including JJ, QY, JN, WH, and CH; and all remaining districts with steady expansion. Considering the above, city expansion could be characterized as a cool center accompanying a hot surrounding area in space, which agrees well with the traditional two-circle pattern of Chengdu city. The centroid analysis results in Fig. 8 indicate that expansion in Chengdu city occurred spatially unbalanced as the gravity center moved notably with a total southeast offset from 2004 to 2018. Therefore, Chengdu city totally expanded toward the southeast, which may be decomposed into southward and eastward expansion. SL expansion yielded the greatest contribution to southward expansion, and eastward expansion primarily determined the overall southern district expansion, including XD, QBJ, and LQY, especially from 2013 to 2018, in which the gravity center of

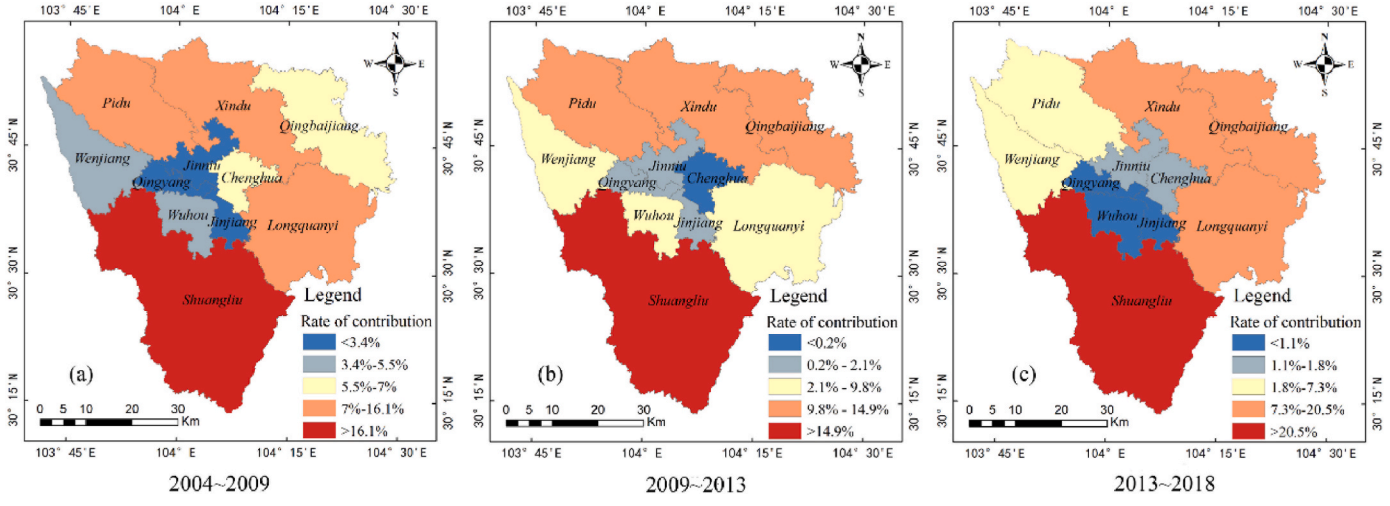

Fig. 8. Built-up area expansion ratio in each district.

Chengdu city experienced an offset of 3608 m, the greatest offset (the central subfigure in Fig. 9). Focusing on each district, Fig. 9(a–k) show unbalanced expansion considering gravity center movement. Compared to the other districts, the gravity centers of QBJ (subfigure c) and SL (subfigure k) exhibited the most notable offsets. Moreover, approximately consistent with the contribution rate to city expansion, the gravity centers of WJ, PD, XD, and LQY moved further than JN, CH, QY, WH and JJ, which are all located at the cool expansion center of Chengdu city. According to the gravity center trajectory in Fig. 9, all gravity centers moved along the major axis of the district polygons, which indicates that the districts of Chengdu city predominantly expanded along the major axis direction from 2004 to 2018. Additionally, the gravity center of the built-up area in each district moved toward the geometric center over time, a stark proof that the urban planning and architectural complex layout in each district became increasingly reasonable and balanced at the district scale.

3.3. Exploration of the urban expansion rationality

The impervious surface area increase was calculated based on the LULC maps, as summarized in Table 6. The built-up area in Chengdu city quintupled from 391.70 km^2 in 2004–2191.70 km^2 in 2018, with a total expansion of 1800 km^2, but the population in the corresponding districts increased by only approximately 2.47 million, which was ~40% of the 2004 population (Table 6). Therefore, an allometric model was introduced to explore the relationship between urban expansion and population growth, examine resource efficiency and further explore the rationality of urban land planning. According to the Chengdu Statistical Yearbook, the allometric model was fitted with the following equation:

Table 6
Impervious surface/built-up area and increase and population information for Chengdu.

Year	Built-up area (km^2)	Population (10000 people)
2004	391.70	604.01
2009	793.86	667.90
2013	1139.19	715.37
2018	2191.70	851.16

$$A = 5.1969e - 10 * P^{4.31042} \quad (20)$$

The fitting equation attained an R-squared value of 0.987 and an F value of 311.08 ($p = 0.0032 < 0.01$) in analysis of variance (ANOVA). The b coefficient of the allometric model ($A = aP^b$) was 4.31, with a T value of 11.04 ($p = 0.0081 < 0.01$) during variable significance testing (T test). The b value was much larger than 0.9, which suggests that positive allometric growth occurred in Chengdu city. This result indicates that the built-up area expansion of Chengdu city was a surplus and excessive for the population increase. Rapid built-up area expansion, accompanied by slower population growth, can cause excessive coverage, extensive land use, and land resource waste. Additionally, the low land use efficiency in Chengdu probably even influenced the urban ecological environment and lowered the quality of life of inhabitants.

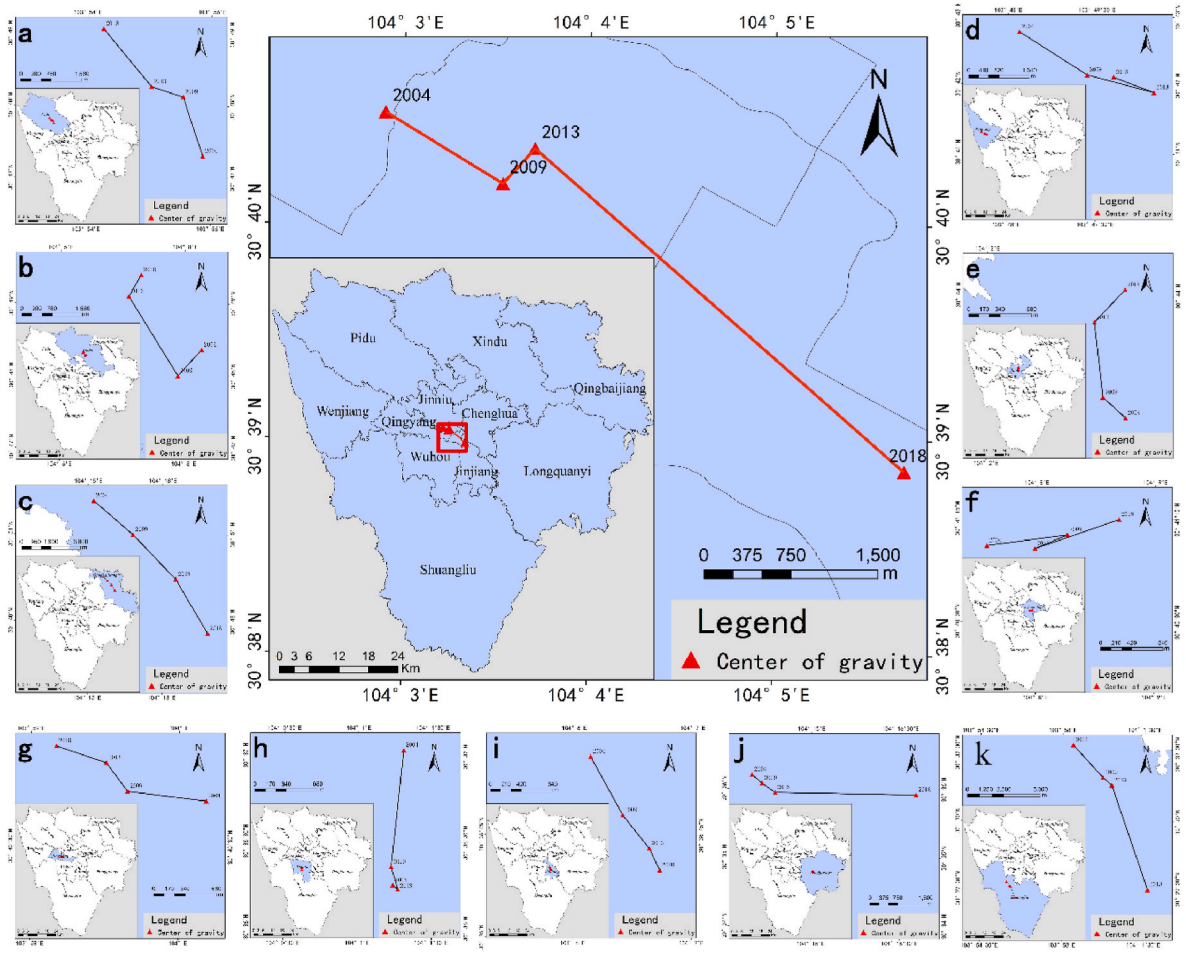

Fig. 9. Gravity center movement in the city from 2004 to 2018. The center indicates the movement in Chengdu city, surrounded by movement maps of the 11 districts: PD (a), XD (b), QBJ (c), WJ (d), JN (e), CH (f), QY (g), WH (h), JJ (i), LQY (j), and SL (k).

3.4. Influence on the urban thermal environment

Based on the TEI images, the thermal environment in Chengdu city was divided according to the six heat island grade levels (Fig. 9): strong cold island, general cold island, colder mid-temperature, hotter mid-temperature, general heat island, and strong heat island zones. From 2004 to 2018, the heated area, including the hotter mid-temperature, general heat island and strong heat island zones, increased from 1668.76 to 1781.34 km^2, and the SUHI phenomenon occurred increasingly frequently in a widespread space, especially strong heat island zone coverage, which was very significant (Fig. 10). According to the area percentage changes (Fig. 11), from 2004 to 2018, the strong cold island and strong heat island zones generally constituted the lowest proportion, the strong cold island zone varied between 4% and 5%, and the strong heat island zone fluctuated at 7%. Compared to the strong cold island and strong heat island zones, the general cold island and general heat island zones attained larger area percentages, ranging from 17% to 19% and 13%–16%, respectively. The colder and hotter mid-temperature zones accounted for the highest area ratios, ranging from 27 to 34% and 25–27%, respectively, which are all areas potentially

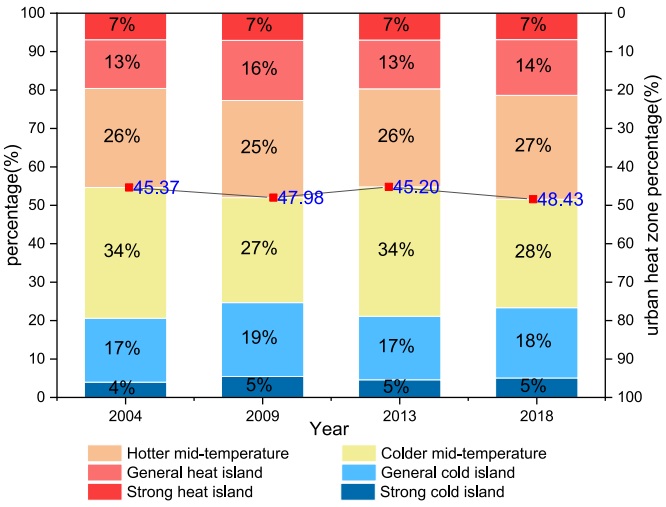

Fig. 11. Area percentage changes at the different heat levels.

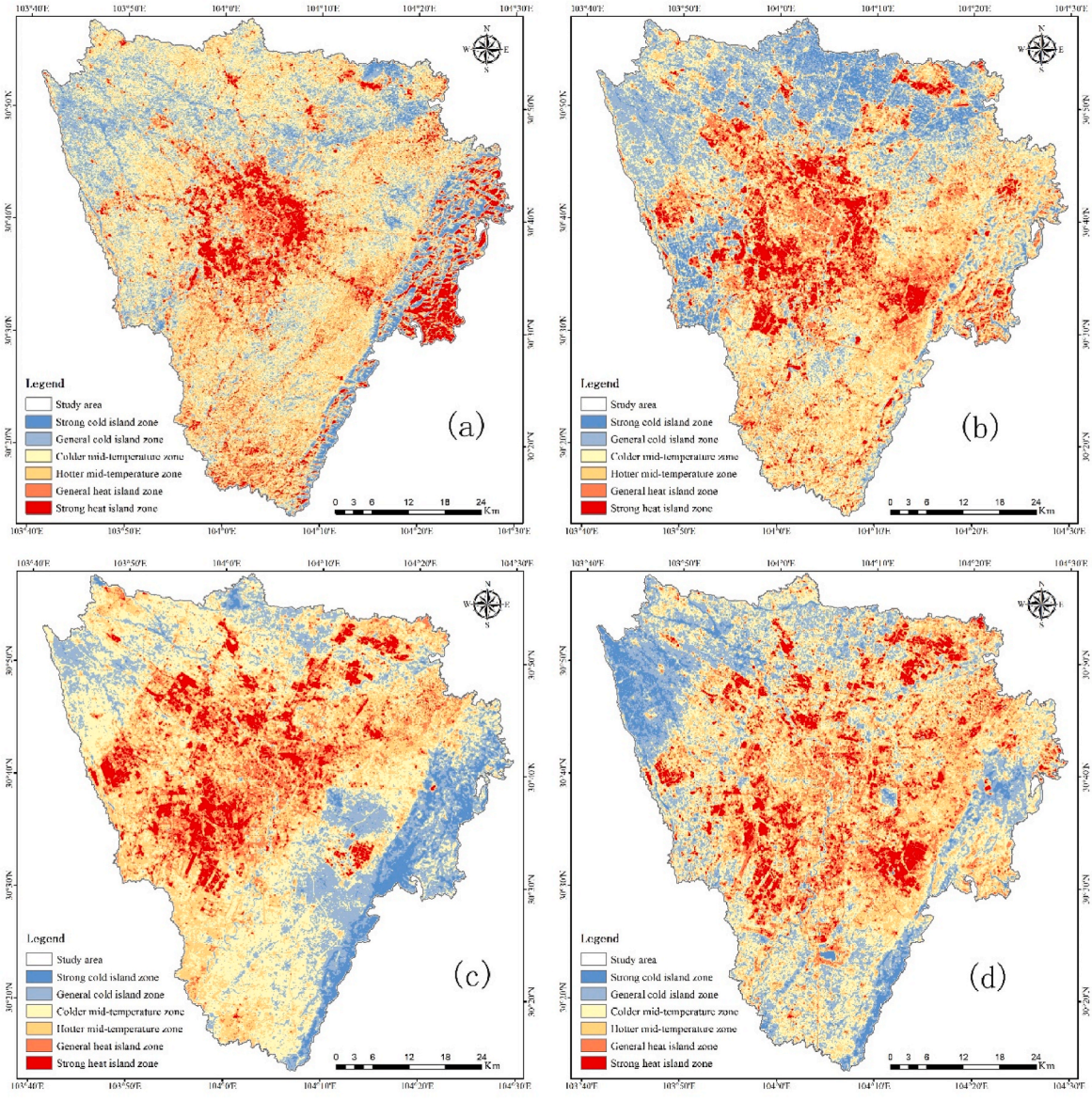

Fig. 10. Distribution of SUHIs in the study area. Subfigures (a) to (d) show 2004, 2009, 2013, and 2018.

degenerating into the hotter mid-temperature zone. The SUHI zone, including the hotter mid-temperature, general heat island and strong heat island zones, generally exhibited a higher trend from 2004 to 2018, and the area percentage increased from 45.37% to 48.43% (Fig. 11). Therefore, the SUHI effect significantly increased and caused increasing urban thermal environmental degradation in Chengdu city.

Furthermore, the relationship between urban thermal environmental degradation and urban expansion was examined by comparing the SUHI changes to the built-up area increase, UGI, the change rate of built-up areas (Rt) and UII, as shown in Fig. 12. The line of SUHI changes indicates that local fluctuations occurred in the overall increasing trend: the SUHI effect increased from 2004 to 2009 with a total area growth of 2.62% in Chengdu city; subsequently, this situation improved with an increase of −2.78% from 2009 to 2013; and unfortunately, these conditions steadily deteriorated with an increase of 3.23% from 2013 to 2018. Fig. 12 indicates that this fluctuation agreed much better with the urban expansion rate and intensity indices Rt and UII than the built-up increase and UGI. Moreover, Correlation analysis indicated that the SUHI was strongly related to Rt and UII with a correlation coefficient >95% (96.77% between SUHI and Rt, 95.69% between SUHI and UII), while built-up area increase and UGI with correlation coefficients of 63.47% and 54.39%, respectively. This great agreement and strong correlation indicate that the urban expansion rate and intensity notably affected the SUHIs in Chengdu city, suggesting that urbanization acceleration creates urban thermal environment risk. Additionally, the turning point from 2009 to 2013 of slow urban expansion (Rt = 43.50%, and UII = 10.87%) accompanied by weakened SUHI effects (−2.78%), indicates that a potential balance between urban expansion and the urban thermal environment can occur, probably by controlling the expansion intensity and optimized urban planning. Compared to the 2004–2009 and 2013–2018 periods, the large conversion (316.44 km^2) from bare soil into vegetation areas as compensation probably alleviated the SUHI effect intensity from 2009 to 2013 because urban vegetation has been verified as a mitigating factor through its increased thermal regulation via evapotranspiration and the provision of shade [68–70]. However, during the next period, 2013–2018, urban expansion increasingly relied on net area conversion from vegetation areas, which sharply reduced the bare soil-provided compensation, leading to a sudden urban thermal environmental deterioration, as indicated by an SUHI area rate increase of 3.23%. Therefore, the LULC conversion pattern in the urbanization process seriously affected the urban thermal environment.

Although China was the most actively-studied country of SUHI researched after 2000, they preferred to focus on large megacities in China [71–74]. A city-based statistical analysis implemented by Zhou et al. [12] has indicated that Beijing, Shanghai, Nanjing, Guangzhou, and Wuhan are the top 5 Chinese cities with the largest number of SUHI studies. Ye et al. [74] explored the urban thermal environment changes during rapid urbanization in the Chinese five largest megacities, Beijing, Tianjin, Shanghai, Guangzhou, and Shenzhen. It is found that those megacities experienced high-speed expansion with a great reduce of urban green space from 2000 to 2010, and from 2010 to 2020, stepped

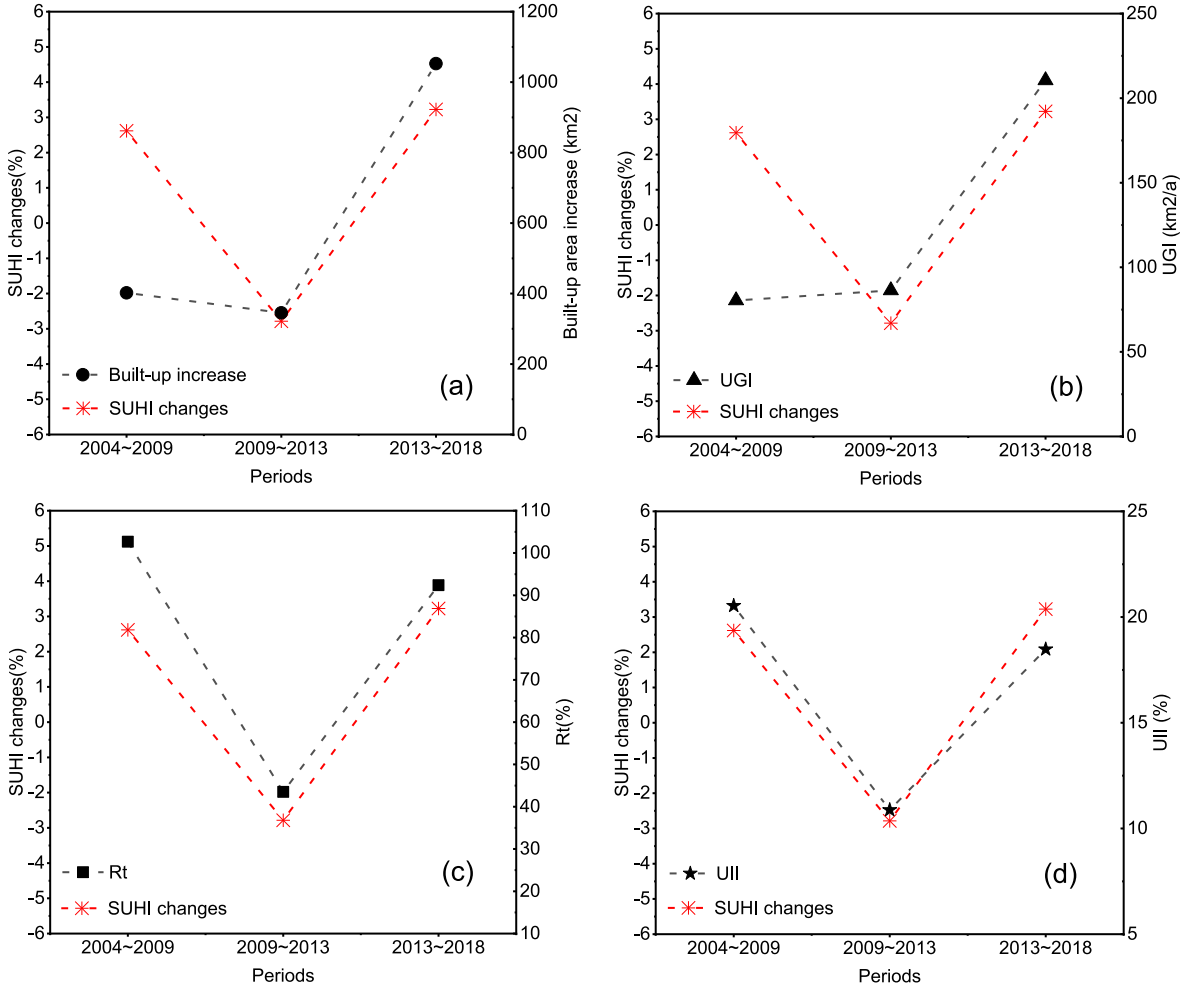

Fig. 12. Relationship between SUHIs and urban expansion. (a) to (d) show the relationship between built-up changes in surface urban heat islands (SUHIs, %) and built-up area increases (km^2), UGI (km^2/a), Rt (%) and UII (%), respectively.

into mature stage of urbanization with a low-speed expansion. In the earlier stages of urbanization, the urban growth can dramatically increase the SUHI extent and intensity, which have also been confirmed in previous study [22,75–77]. While in the mature stage of urbanization, the urbanization effect on SUHI becomes gentle, and is mostly regulated by the cooling effect of the increasing urban green space. According to the impervious surface expansion and LULC changes from 2004 to 2018, Chengdu city, located at the relatively undeveloped Southwest China, step into the earlier stages of urbanization after 2013, which means Chengdu city steps into high-speed expansion stages later a decade or later than those developed large megacities in China. In this stage, it is a severe test to relieve the drastic SHUI effects, one intractable eco-environmental consequences of urbanization. It has been demonstrated that ecological land, including water bodies, forest, farmland and urban green space, have a positive effect on mitigating the region's high temperature [12,76]. Therefore, optimizing the landscape composition and spatial configuration, is the most probable and effective way for practitioners to formulate the associated mitigation and adaptation strategies.

4. Conclusions

According to the urban expansion spatiotemporal characteristics detected with the Landsat-LULC classification results, the urbanization pattern was examined to analyze the expansion rationality and further explore the effect on the urban thermal environment reflected by the LST data retrieved from Landsat images. Our results reveal that from 2004 to 2018, urban expansion in Chengdu city exhibited overall imbalance in time and space, and the gravity center of each district mostly exhibited a notable offset toward the district center, leading to local district balance development. The source of urban expansion changed from the dominant conversion from bare soil in the 2004–2009 period to a considerable conversion from bare soil and vegetation areas in the 2009–2013 period, then to absolute dominant conversion (85%) from vegetation in the 2013–2018 period, stepped into early urbanization stage with high-speed urban expansion. Based on model analysis, urban expansion in Chengdu city experienced an excessive urbanization pattern, and urban expansion far extended beyond the scope of urban population growth demands. In contrast, based on an analysis of SUHI changes with the urban expansion rate and intensity, urban sprawl imposed a serious promoting effect on SUHI acceleration in Chengdu city. Moreover, during recent rapid urbanization in Chengdu, the increasing reliance on conversion from vegetation areas, the effective and typical urban element weakening and moderating SUHIs, further accelerated SUHI effects. As a result, excess expansion occurred at the expense of harm to the urban ecological and thermal environments in Chengdu city, which further threatened the quality of life and human health of residents from the aspects of energy consumption, air and water quality, living comfort, and increasing thermal-related disease risks. Therefore, land use strategy and urban planning efforts should be optimized and revised consistently to achieve a balance among urbanization, population increase, urban ecological and thermal environment, and prevent extensive land use and land resource waste, which are crucial to ensure urban health and ecology and increase the environment's robustness to global climate change and frequent local extreme meteorological disasters.

CRediT authorship contribution statement

Wenping Yu: Writing – review & editing, Writing – original draft, Visualization, Project administration, Methodology, Formal analysis, Data curation, Conceptualization. **Jinan Shi:** Visualization, Validation, Software, Data curation. **Yuling Fang:** Validation, Software, Methodology, Formal analysis, Data curation. **Aimeng Xiang:** Validation, Software, Resources, Methodology, Investigation. **Xiang Li:** Software, Resources, Investigation, Data curation. **Chunhong Hu:** Visualization, Validation, Software, Methodology, Formal analysis. **Mingguo Ma:** Writing – review & editing, Supervision, Resources, Project administration, Funding acquisition, Conceptualization.

Declaration of competing interest

The authors declare that they have no known competing financial interests or personal relationships that could have appeared to influence the work reported in this paper.

Acknowledgments

This study was supported by the National Natural Science Foundation of China (Grant No. 42171338), National Major Projects on High-Resolution Earth Observation System (Grant No. 21-Y20B01-9001-19/22) and the China Postdoctoral Science Foundation (grant number: 2020M670542).

References

[1] S. Angel, J. Parent, D.L. Civco, A. Blei, D. Potere, The dimensions of global urban expansion: estimates and projections for all countries, 2000–2050, Prog. Plann. 75 (2011) 53–107.
[2] G. Chen, X. Li, X. Liu, Y. Chen, X. Liang, J. Leng, X. Xu, W. Liao, Y.a. Qiu, Q. Wu, K. Huang, Global projections of future urban land expansion under shared socioeconomic pathways, Nat. Commun. 11 (2020) 537.
[3] H. Chen, G.Q. Chen, X. Ji, Cosmic emergy based ecological systems modelling, Commun. Nonlinear Sci. Numer. Simulat. 15 (2010) 2672–2700.
[4] P. Mondal, J. Southworth, Evaluation of conservation interventions using a cellular automata-Markov model, For. Ecol. Manag. 260 (2010) 1716–1725.
[5] X.X. Zhu, C. Qiu, J. Hu, Y. Shi, Y. Wang, M. Schmitt, H. Taubenböck, The urban morphology on our planet – global perspectives from space, Rem. Sens. Environ. 269 (2022), 112794.
[6] A. Erol, K. Ekinci, D. Akbolat, F. Evrendilek, Modeling impacts of land uses on carbon and nitrogen contents, carbon dioxide and water effluxes of Mediterranean soils, Pol. J. Environ. Stud. 25 (2016).
[7] J. Li, C. Song, L. Cao, F. Zhu, X. Meng, J. Wu, Impacts of landscape structure on surface urban heat islands: a case study of Shanghai, China, Rem. Sens. Environ. 115 (2011) 3249–3263.
[8] S. Merte, Estimating heat wave-related mortality in Europe using singular spectrum analysis, Climatic Change 142 (2017) 321–330.
[9] L. Zhao, X. Lee, R.B. Smith, K. Oleson, Strong contributions of local background climate to urban heat islands, Nature 511 (2014) 216.
[10] J.A. Voogt, T.R. Oke, Thermal remote sensing of urban climates, Rem. Sens. Environ. 86 (2003) 370–384.
[11] Q. Weng, Thermal infrared remote sensing for urban climate and environmental studies: methods, applications, and trends, ISPRS J. Photogrammetry Remote Sens. 64 (2009) 335–344.
[12] D. Zhou, J. Xiao, S. Bonafoni, C. Berger, K. Deilami, Y. Zhou, S. Frolking, R. Yao, Z. Qiao, J.A.J.R.S. Sobrino, Satellite remote sensing of surface urban heat islands: progress, challenges, and perspectives 11 (2019) 48.
[13] S. Chapman, J.E.M. Watson, A. Salazar, M. Thatcher, C.A. McAlpine, The impact of urbanization and climate change on urban temperatures: a systematic review, Landsc. Ecol. 32 (2017) 1921–1935.
[14] H. Du, D. Wang, Y. Wang, X. Zhao, F. Qin, H. Jiang, Y. Cai, Influences of land cover types, meteorological conditions, anthropogenic heat and urban area on surface urban heat island in the Yangtze River Delta Urban Agglomeration, Sci. Total Environ. 571 (2016) 461–470.
[15] L. Mariani, S.G. Parisi, G. Cola, R. Lafortezza, G. Colangelo, G. Sanesi, Climatological analysis of the mitigating effect of vegetation on the urban heat island of Milan, Italy, Sci. Total Environ. 569 (2016) 762–773.
[16] J. Peng, J. Ma, Q. Liu, Y. Liu, Y.n. Hu, Y. Li, Y. Yue, Spatial-temporal change of land surface temperature across 285 cities in China: an urban-rural contrast perspective, Sci. Total Environ. 635 (2018) 487–497.
[17] K.C. Seto, M. Fragkias, B. Guneralp, M.K. Reilly, A Meta-analysis of global urban land expansion, PLoS One 6 (2011).
[18] W. Kuang, J. Liu, J. Dong, W. Chi, C. Zhang, The rapid and massive urban and industrial land expansions in China between 1990 and 2010: a CLUD-based analysis of their trajectories, patterns, and drivers, Landsc. Urban Plann. 145 (2016) 21–33.
[19] K.C. Seto, B. Guneralp, L.R. Hutyra, Global forecasts of urban expansion to 2030 and direct impacts on biodiversity and carbon pools, Proc. Natl. Acad. Sci. U.S.A. 109 (2012) 16083–16088.
[20] B. Shi, C.-S. Tang, L. Gao, C. Liu, B.-J. Wang, Observation and analysis of the urban heat island effect on soil in Nanjing, China, Environ. Earth Sci. 67 (2012) 215–229.
[21] X. Wang, X. Sun, J. Tang, X. Yang, Urbanization-induced regional warming in Yangtze River Delta: potential role of anthropogenic heat release, Int. J. Climatol. 35 (2015) 4417–4430.

[22] Z. Yu, X. Guo, Y. Zeng, M. Koga, H. Vejre, Variations in land surface temperature and cooling efficiency of green space in rapid urbanization: the case of Fuzhou city, China, Urban For. Urban Green. 29 (2018) 113–121.
[23] R. Yao, Q. Luo, Z. Luo, L. Jiang, Y. Yang, An integrated study of urban microclimates in Chongqing, China: historical weather data, transverse measurement and numerical simulation, Sustain. Cities Soc. 14 (2015) 187–199.
[24] C. Liu, Q. Zhang, H. Luo, S. Qi, S. Tao, H. Xu, Y. Yao, An efficient approach to capture continuous impervious surface dynamics using spatial-temporal rules and dense Landsat time series stacks, Rem. Sens. Environ. 229 (2019) 114–132.
[25] H. Shih, D.A. Stow, J.R. Weeks, L.L. Coulter, Determining the type and starting time of land cover and land use change in southern Ghana based on discrete analysis of dense landsat image time series, IEEE J. Sel. Top. Appl. Earth Obs. Rem. Sens. 9 (2016) 2064–2073.
[26] C. Wu, A.T. Murray, Estimating impervious surface distribution by spectral mixture analysis, Rem. Sens. Environ. 84 (2003) 493–505.
[27] D. Lu, Q. Weng, Urban classification using full spectral information of landsat ETM + imagery in Marion county, Indiana, Photogramm. Eng. Rem. Sens. 71 (2005) 1275–1284.
[28] M.K. Ridd, Exploring a V-I-S (vegetation-impervious surface-soil) model for urban ecosystem analysis through remote sensing: comparative anatomy for cities†, Int. J. Rem. Sens. 16 (1995) 2165–2185.
[29] H.C. Shih, D.A. Stow, Y.M. Tsai, D.A. Roberts, Estimating the starting time and identifying the type of urbanization based on dense time series of landsat-derived Vegetation-Impervious-Soil (V-I-S) maps - a case study of North Taiwan from 1990 to 2015, Int. J. Appl. Earth Obs. Geoinf. 85 (2020) 11.
[30] S.L. Powell, W.B. Cohen, Z. Yang, J.D. Pierce, M. Alberti, Quantification of impervious surface in the Snohomish water resources inventory area of western Washington from 1972–2006, Rem. Sens. Environ. 112 (2007) 1895–1908.
[31] X. Zhang, D. Pan, J. Chen, Y. Zhan, Z. Mao, Using long time series of Landsat data to monitor impervious surface dynamics: a case study in the Zhoushan Islands, J. Appl. Remote Sens. 7 (2013), 073515-073515.
[32] H.Q. Ha, Mapping Impervious Surface in the Greater Hanoi Area, Vietnam from Time Series Landsat Images 1988-2015, and Assessing its Impacts on Surface Runoff, Indiana State University, 2017.
[33] C. Deng, Z. Zhu, Continuous subpixel monitoring of urban impervious surface using landsat time series, Rem. Sens. Environ. (2018), 110929.
[34] Z.-L. Li, B.-H. Tang, H. Wu, H. Ren, G. Yan, Z. Wan, I.F. Trigo, J.A. Sobrino, Satellite-derived land surface temperature: current status and perspectives, Rem. Sens. Environ. 131 (2013) 14–37.
[35] K. Mao, H.J. Tang, Z.X. Chen, Y.B. Qiu, Z. Qin, M.C. Li, A split-window algorithm for retrieving land surface temperature from ASTER data, Remote Sens. Inf. 5 (2006) 7–10.
[36] Z.-h. Qin, A. Karnieli, P. Berliner, A mono-window algorithm for retrieving land surface temperature from Landsat TM data and its application to the Israel-Egypt border region, Int. J. Rem. Sens. 22 (2001) 3719–3746.
[37] A. Sekertekin, S. Bonafoni, Land surface temperature retrieval from landsat 5, 7, and 8 over rural areas: assessment of different retrieval algorithms and emissivity models and toolbox implementation, Rem. Sens. 12 (2020).
[38] J.A. Sobrino, J.C. Jiménez-Muñoz, Land surface temperature retrieval from thermal infrared data: an assessment in the context of the Surface Processes and Ecosystem Changes through Response Analysis (SPECTRA) mission, J. Geophys. Res. Atmos. (2005) 110, 1984–2012.
[39] Z. Wan, Y. Zhang, Q. Zhang, Z.-l. Li, Validation of the land-surface temperature products retrieved from terra moderate resolution imaging Spectroradiometer data, Rem. Sens. Environ. 83 (2002) 163–180.
[40] Z.M. Wan, J. Dozier, A generalized split-window algorithm for retrieving land-surface temperature from space, IEEE Trans. Geosci. Rem. Sens. 34 (1996) 892–905.
[41] W. Yu, M. Ma, H. Yang, J. Tan, X. Li, Supplement of the radiance-based method to validate satellite-derived land surface temperature products over heterogeneous land surfaces, Rem. Sens. Environ. 230 (2019), 111188.
[42] Y. Deng, S. Wang, X. Bai, Y. Tian, L. Wu, J. Xiao, F. Chen, Q. Qian, Relationship among land surface temperature and LUCC, NDVI in typical karst area, Sci. Rep. 8 (2018) 641.
[43] L. Liu, Y. Zhang, Urban heat island analysis using the Landsat TM data and ASTER data: a case study in Hong Kong, Rem. Sens. 3 (2011) 1535–1552.
[44] N. Schwarz, S. Lautenbach, R. Seppelt, Exploring indicators for quantifying surface urban heat islands of European cities with MODIS land surface temperatures, Rem. Sens. Environ. 115 (2011) 3175–3186.
[45] I.P. Senanayake, W. Welivitiya, P.M. Nadeeka, Remote sensing based analysis of urban heat islands with vegetation cover in Colombo city, Sri Lanka using Landsat-7 ETM+ data, Urban Clim. 5 (2013) 19–35.
[46] M. Esad, H. Md Obaidul, M. Nischal, Radiometric calibration updates to the Landsat collection, in: Proc.SPIE, 2016.
[47] A.D. Gerace, M. Montanaro, Derivation and validation of the stray light correction algorithm for the thermal infrared sensor onboard landsat 8, Rem. Sens. Environ. 191 (2017) 246–257.
[48] R. Niclòs, J. Puchades, C. Coll, M.J. Barberà, L. Pérez-Planells, J.A. Valiente, J. M. Sánchez, Evaluation of Landsat-8 TIRS data recalibrations and land surface temperature split-window algorithms over a homogeneous crop area with different phenological land covers, ISPRS J. Photogrammetry Remote Sens. 174 (2021) 237–253.
[49] M. Paul, S. Florian, Comparasion of NDBI and NDVI as Indicators of Surface Urban Heat Island Effect in Landsat 8 Imagery: A Case Study of Iasi, Present Environ. Sustain. Dev. vol. 11 (2017) 141–150.
[50] J.W. Rouse Jr., R.H. Haas, J.A. Schell, D.W. Deering, Monitoring the Vernal Advancement and Retrogradation (Green Wave Effect) of Natural Vegetation, 1973.
[51] Y. Zha, J. Gao, S. Ni, Use of normalized difference built-up index in automatically mapping urban areas from TM imagery, Int. J. Rem. Sens. 24 (2003) 583–594.
[52] X.U. Han-Qiu, A study on information extraction of water body with the modified normalized difference water index (MNDWI), J. Rem. Sens. 5 (2005) 589–595.
[53] S.K. McFeeters, The use of the Normalized Difference Water Index (NDWI) in the delineation of open water features, Int. J. Rem. Sens. 17 (1996) 1425–1432.
[54] Y. Haibo, W. Zongmin, Z. Hongling, G. Yu, Water body extraction methods study based on RS and GIS, Proc. Environ. Sci. 10 (2011) 2619–2624.
[55] Y. Li, G. Liu, Characterizing spatiotemporal pattern of land use change and its driving force based on GIS and landscape analysis techniques in Tianjin during 2000–2015, Sustainability 9 (2017) 894.
[56] Y. Chen, Y. Zhou, Researches in models of allometric analysis of urban systems and forecast of urbanization level based on RS data of urban area, Acta Sci. Nauralium Univ. Pekin. 37 (2001) 819–826.
[57] C. Molinero, S. Thurner, How the Geometry of Cities Explains Urban Scaling Laws and Determines Their Exponents, 2019 *arXiv preprint arXiv:1908.07470*.
[58] W.B. Tan, B. Liu, Z.X. Zhang, W. Ling, Remote sensing monitoring and analyzing of the urban built-up land expansion in Kunming in 1974–2004, Geo Inf. Sci. 11 (2009) 117–124.
[59] L. Wang, H. Xu, S. Li, Dynamic monitoring of the urban expansion in Fuzhou of SE China using remote sensing technology [J], Geo Inf. Sci. 4 (2006).
[60] T. Wang, B. Li, L. He, P. Yu, Y. Zhang, F. Xiao, X. Wang, Analysis of spatial-temporal characteristics of urban expansion and driving forces in Xi'an, Sci. Surv. Mapp. 13 (2017).
[61] J. Sobrino, N. Raissouni, Toward remote sensing methods for land cover dynamic monitoring: application to Morocco, Int. J. Rem. Sens. 21 (2000) 353–366.
[62] Z.-h. Qin, W.-j. Li, B. Xu, W. Zhang, Estimation method of land surface emissivity for retrieving land surface temperature from Landsat TM6 data, Adv. Mar. Sci. 22 (2004) 129–137.
[63] J.A. Sobrino, J.C. Jiménez-Muñoz, L. Paolini, Land surface temperature retrieval from LANDSAT TM 5, Rem. Sens. Environ. 90 (2004) 434–440.
[64] J.A. Sobrino, J.C. Jiménez-Muñoz, G. Sòria, M. Romaguera, L. Guanter, J. Moreno, A. Plaza, P. Martínez, Land surface emissivity retrieval from different VNIR and TIR sensors, IEEE Trans. Geosci. Rem. Sens. 46 (2008) 316–327.
[65] L. Jiao, G. Xu, J. Jin, T. Dong, J. Liu, Y. Wu, B. Zhang, Remotely sensed urban environmental indices and their economic implications, Habitat Int. 67 (2017) 22–32.
[66] S. Chen, T. Wang, Comparison analyses of equal interval method and mean-standard deviation method used to delimitate urban heat island: comparison analyses of equal interval method and mean-standard deviation method used to delimitate urban heat island, Geo Inf. Sci. 11 (2009) 145–150.
[67] Q. Lang, W. Yu, M. Ma, J. Wen, Analysis of the spatial and temporal evolution of land cover and heat island effects in six districts of Chongqing's main city, Sensors 19 (2019).
[68] P. Kabano, S. Lindley, A. Harris, Evidence of urban heat island impacts on the vegetation growing season length in a tropical city, Landsc. Urban Plann. 206 (2021), 103989.
[69] B.A. Norton, A.M. Coutts, S.J. Livesley, R.J. Harris, A.M. Hunter, N.S.G. Williams, Planning for cooler cities: a framework to prioritise green infrastructure to mitigate high temperatures in urban landscapes, Landsc. Urban Plann. 134 (2015) 127–138.
[70] C.I. Portela, K.G. Massi, T. Rodrigues, E. Alcântara, Impact of urban and industrial features on land surface temperature: evidences from satellite thermal indices, Sustain. Cities Soc. 56 (2020), 102100.
[71] H. Liu, B. Huang, Q. Zhan, S. Gao, R. Li, Z. Fan, The influence of urban form on surface urban heat island and its planning implications: evidence from 1288 urban clusters in China, Sustain. Cities Soc. 71 (2021), 102987.
[72] Q. Meng, L. Zhang, Z. Sun, F. Meng, L. Wang, Y. Sun, Characterizing spatial and temporal trends of surface urban heat island effect in an urban main built-up area: a 12-year case study in Beijing, China, Rem. Sens. Environ. 204 (2018) 826–837.
[73] Z. Qiao, G. Tian, L. Zhang, X. Xu, Influences of urban expansion on urban heat island in Beijing during 1989–2010, Adv. Meteorol. 2014 (2014), 187169.
[74] H. Ye, Z. Li, N. Zhang, X. Leng, D. Meng, J. Zheng, Y. Li, Variations in the effects of landscape patterns on the urban thermal environment during rapid urbanization (1990–2020) in megacities, Rem. Sens. 13 (2021).
[75] Y.-C. Chen, H.-W. Chiu, Y.-F. Su, Y.-C. Wu, K.-S. Cheng, Does urbanization increase diurnal land surface temperature variation? Evidence and implications, Landsc. Urban Plann. 157 (2017) 247–258.
[76] J. Peng, P. Xie, Y. Liu, J. Ma, Urban thermal environment dynamics and associated landscape pattern factors: a case study in the Beijing metropolitan region, Rem. Sens. Environ. 173 (2016) 145–155.
[77] M. Ranagalage, R.C. Estoque, X. Zhang, Y. Murayama, Spatial changes of urban heat island formation in the Colombo District, Sri Lanka: implications for sustainability planning, Sustainability 10 (2018) 1367.